

Switching Magnetic Anisotropy of SrRuO₃ by Capping-Layer-Induced Octahedral Distortion

Shan Lin,^{1,2} Qinghua Zhang,¹ Manuel A. Roldan,³ Sujit Das,⁴ Timothy Charlton,⁵ Michael R. Fitzsimmons,^{5,6} Qiao Jin,^{1,2} Sisi Li,⁷ Zhenping Wu,⁷ Shuang Chen,⁸ Haizhong Guo,⁸^{*}, Xin Tong,⁹ Meng He,¹ Chen Ge,¹⁰ Can Wang,^{1,2,10} Lin Guo,^{1,2,10} Kui-juan Jin,^{1,2,10,*} and Er-Jia Guo,^{1,2,10,†}

¹*Beijing National Laboratory for Condensed Matter Physics and Institute of Physics, Chinese Academy of Sciences, Beijing 100190, China*

²*University of Chinese Academy of Sciences, Beijing 100049, China*

³*Eyring Materials Center, Arizona State University, Tempe, Arizona 85287, USA*

⁴*Department of Materials Science and Engineering, University of California, Berkeley, California 94720, USA*

⁵*Neutron Scattering Division, Oak Ridge National Laboratory, Oak Ridge 37831, USA*

⁶*Department of Physics and Astronomy, University of Tennessee, Knoxville, Tennessee 37996, USA*

⁷*State Key Laboratory of Information Photonics and Optical Communications & Laboratory of Optoelectronics Materials and Devices, School of Science, Beijing University of Posts and Telecommunications, Beijing 100876, China*

⁸*School of Physical Engineering, Zhengzhou University, Zhengzhou 450001, China*

⁹*China Spallation Neutron Source, Institute of High Energy Physics, Chinese Academy of Sciences, Beijing 10049, China*

¹⁰*Songshan Lake Materials Laboratory, Dongguan, Guangdong 523808, China*

(Received 12 November 2019; revised manuscript received 30 December 2019; accepted 14 February 2020; published 12 March 2020)

Materials with large perpendicular magnetic anisotropy (PMA) are candidates for spintronic devices, such as magnetic random-access memory, etc., due to their stable magnetic reference states. Because of shape anisotropy, the magnetic easy axis of oxide thin films favors in-plane orientation. In this Paper, we demonstrate a convenient means to control the magnetic anisotropy of SrRuO₃ (SRO) ultrathin layers from in-plane to out-of-plane by capping with nonmagnetic materials. Tuning the anisotropy is achieved by imposition of symmetry mismatch at the interface-induced structural transition of SRO with suppressed octahedral tilt. These results suggest a potential direction for engineering magnetic oxide thin films with flexible tunable PMA using capping-layer-induced dissimilar symmetry.

DOI: 10.1103/PhysRevApplied.13.034033

I. INTRODUCTION

Magnetic ultrathin layers with strong out-of-plane magnetization, i.e., perpendicular magnetic anisotropy (PMA), have extremely high-value research compared to in-plane anisotropy in magnetic recording media, spin valves, magnetic tunnel junctions, etc. [1–5]. From the practical device point of view, it is easier, faster, and more energetically efficient for out-of-plane magnetization reversal than in-plane magnetization reversal [6,7] using low power-consumed optical pumping [8] and current-driven spin-orbital torques [9,10]. Moreover, competition between PMA and dipolar interactions enables the formation of magnetic skyrmions with topological protection [11–13]

and stabilization of chiral spin textures, for instance, magnetic iron garnets [14,15] due to the presence of interfacial Dzyaloshinskii-Moriya (DM) interaction. The small size and low-energy consumption of skyrmions make them extremely promising candidates for future high-density data storage and processing.

Many intriguing spintronic phenomena have been discovered in transition-metal-oxide (TMO) thin films, including the (inverse) spin Hall effect [16,17], the topological Hall effect [18–20], etc. Yet, for most magnetic oxide films, shape anisotropy dominates over magnetoelectric anisotropy, and thus the in-plane orientation of magnetic moment is energetically favorable. The easy axis aligns naturally along the in-plane direction in oxide thin films. From an application point of view, in-plane magnetization reversal is less desirable than the out-of-plane one [6–10]. Thus, control of the magnetization orientation

*kjjin@iphy.ac.cn

†ejguo@iphy.ac.cn

in oxide thin films to present PMA is an outstanding challenge.

In strongly correlated electron systems, the magnetic ground state is coupled to structural degrees of freedom. Thus, by manipulating the structure via stress, the magnetic ground state can be affected. As an example, bulk SrRuO₃ (SRO) is a ferromagnetic metal with an ordered magnetic moment of approximately 1.6 μ_B/Ru [21,22]. SRO is widely used as an electrode material in ferroelectric field-effect transistors or tunneling junctions due to its compatible crystal structure and lattice parameter [23–25]. SRO also exhibits interesting physics and shows a large magnetoelastic response [26,27]. Recently, nanoscale topologically protected whirling spin texture was reported in SRO ultrathin layers triggered by the ferroelectric proximity effect [19]. The minor change of ionic displacements in SRO could stabilize the emergent spin texture. By switching the polarity of capped ferroelectrics, i.e., reversal of the ionic displacement, the density and thermodynamic stability of magnetic skyrmionlike structures can be reversibly controlled. These phenomena indicate that the intriguing magnetic properties of SRO thin films are strongly coupled with their structural parameters.

Previous work demonstrated the physical properties of SRO single layers strongly depended on the substrate-induced strain [28–32] and crystallographic orientations [33,34], namely “epitaxial strain engineering.” In the three-dimensional network of corner-sharing oxygen octahedrons in perovskite oxides, the elastic strain of a thin film modifies the bonding angle, octahedral tilt, and even the type of rotation pattern in a nontrivial way. The degree of electron correlations is readily changed by an alternative means—“symmetry engineering” through effectively modifying the oxygen octahedral distortions [35–40]. This effect can be imposed directly from the selected substrates, like NdGaO₃ with $a^-a^-c^+$ rotation in Glazer notation [36–40] or underlayers [41] by engineering the oxygen coordination environment before thin-film growth. However, the question of how the rotation pattern transferred from the capping layer to the bottom layer accommodates the elastic stress is raised. Earlier work showed an increase in the Curie temperature (T_C) of the SRO layer after an SrTiO₃ layer is capped and attributed to the suppression of octahedral rotations [42]. Here, we investigate the magnetic anisotropy of SRO by capping a nonmagnetic LaNiO₃ (LNO) layer on top. LNO is chosen because it exhibits an octahedral rotation of $a^-a^-a^-$ with $R\bar{3}c$ symmetry [43], in contrast to that of bulk SRO with rotation pattern $a^-a^-c^+$ and orthorhombic lattice structure [35–40]. Note only one coordinate axis has a different rotation pattern between LNO/SRO, allowing us to simplify the understanding of octahedral distortion effect to their physical properties.

In this paper, we report a simple means to control the magnetic anisotropy of SRO ultrathin films effectively

using interfacial symmetry mismatch. Capped by an ultra-thin nonmagnetic LNO layer with dissimilar crystallographic symmetry from SRO, the magnetic easy axis of SRO switches from in-plane to out-of-plane direction, and the conductivity is significantly improved. Using XRD and STEM, we show that the LNO capping layer suppresses the oxygen octahedral tilt in SRO, even though the in-plane epitaxial strain remains. This approach suggests a potential direction for designing magnetic epitaxial thin films with flexible tunable PMA using symmetry engineering.

II. EXPERIMENT AND METHODS

A. Sample growth and transport measurement

The SRO single layers and LNO/SRO bilayers are grown on (001)-oriented STO substrates by pulsed-laser deposition. Before thin-film deposition, STO substrates are treated by buffered hydrofluoric acid and subsequently annealed at 1050 °C for 2 h to produce atomically flat surfaces with TiO₂ termination. During film growth, the substrate temperature is kept at 700 °C and the oxygen partial pressure is maintained at 100 mTorr. The growth process and layer thickness are monitored by *in situ* RHEED, as shown in Fig. 1(a). The thickness of the SRO layer is 12 u.c. (approximately 5 nm) in order to keep a good conductivity and magnetization. A 6-u.c.- (approximately 2 nm) thick LNO layer is deposited on top of the SRO layer to study the interfacial symmetry effect. For neutron reflectivity measurements, the thickness of the LNO capping layer is 25 u.c. (approximately 9 nm). X-ray reflectivity (XRR) measurements are performed to check the layer thickness. The morphologies of STO substrates and as-grown samples are measured by an atomic force microscope (MFP-3D, Asylum Research). Atomic-force-microscopy measurements confirm the terraced surfaces on the as-grown samples (see Fig. S1 in the Supplemental Material [44]). The good crystallinity of our samples is confirmed by XRD θ -2 θ and rocking-curve scans. The crystallographic symmetry of SRO layers is examined by XRD reciprocal space mapping (RSM) [44]. Electrical transport measurements are performed using a physical property measurement system (PPMS). The magnetic properties of our samples are recorded using a superconducting quantum interference device (SQUID) magnetometer equipped with a rotational stage in the vacuum cryostats.

B. High-resolution STEM measurements

SRO single layer and LNO/SRO bilayer specimens are prepared by standard focused-ion-beam lift-out technique. The LNO/SRO bilayer is measured using a JEM ARM 200F transmission electron microscope at Eyring Materials Center of Arizona State University. A SRO single layer is investigated using a JEM ARM 200CF microscope at the Institute of Physics of Chinese Academy of

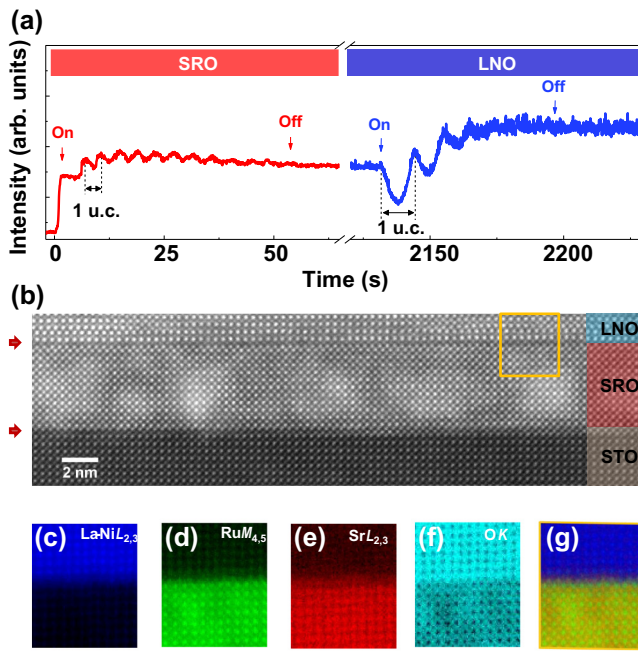


FIG. 1. Growth and structural characterization of the LaNiO₃/SrRuO₃ (LNO/SRO) bilayer. (a) RHEED oscillations monitored during film growth. One oscillation represents the deposition of one u.c. (b) Atomic resolution STEM HAADF image of the LNO/SRO bilayer grown on a STO substrate observed along the [100] orientation. Red arrows marked the positions of the heterointerfaces. (c)–(f) STEM EELS maps for LaNi-L_{2,3}, Ru-M_{4,5}, Sr-L_{2,3}, O-K edges, respectively, acquired from an orange rectangle area marked in (b). (g) Mixed-color EELS map with the integrated intensities from all elements.

Sciences. Both electron microscopes operate at 200 kV and are equipped with double spherical aberration (Cs) correctors. The atomic resolution high-angle annular dark field (HAADF) and annular bright-field (ABF) images are obtained for both samples. STEM electron energy-loss spectroscopy (EELS) measurements are conducted on the LNO/SRO bilayer. The elemental-specific EELS maps have are produced by integrating the signals from interested regions after background subtracting using a power law.

C. Polarized neutron reflectometry measurements

A polarized neutron reflectometry (PNR) experiment on the LNO/SRO bilayer is performed on the Magnetism Reflectometer (BL-4A) at Spallation Neutron Source (SNS) of Oak Ridge National Laboratory (ORNL). The bilayer is field cooled to 25 K with an in-plane magnetic field of 1 T. The neutron reflectivity is recorded as a function of the scattering vector, $q = 4\pi \sin(\theta_i)/\lambda$, for the spin-up (R^+) and spin-down (R^-) polarized neutrons, where λ is the neutron wavelength, and θ_i is the incident angle, respectively. The difference between neutron reflectivities from R^+ and R^- is a non-zero value related

to the magnetization depth profile. SA is calculated by $(R^+ - R^-)/(R^+ + R^-)$. The PNR data is fitted using a chemical depth profile obtained from XRR fitting. We use NIST RefID program to fit all reflectivity data [45].

III. RESULTS AND DISCUSSION

A. Rotating the magnetic anisotropy of SRO ultrathin films

An atomic resolution STEM-HAADF image of the LNO/SRO bilayer is shown in Fig. 1(b), confirming the thickness of SRO and LNO ultrathin layers in design and the epitaxial growth of the high-quality heterostructure with atomically sharp interfaces. Compositional EELS maps obtained from the analysis of LaNi-L_{2,3}, Ru-M_{4,5}, Sr-L_{2,3}, O-K signals are shown in Figs. 1(c)–1(f), respectively. A mixed-color EELS map with integrated intensities from all elements is shown in Fig. 1(g). The bilayer sample shows a uniform chemical distribution within each layer and chemical intermixing is limited to about one-unit cell for both SRO/STO and SRO/LNO interfaces.

Figures 2(a) and 2(b) show M - H curves of the SRO single layer and the LNO/SRO bilayer when $H \parallel ab$ and $H \parallel c$ at 25 K, respectively. The saturation magnetizations (M_s) of the SRO single layer is approximately $1.25 \mu_B/\text{Ru}$, which is approximately 32% smaller than that of the LNO/SRO

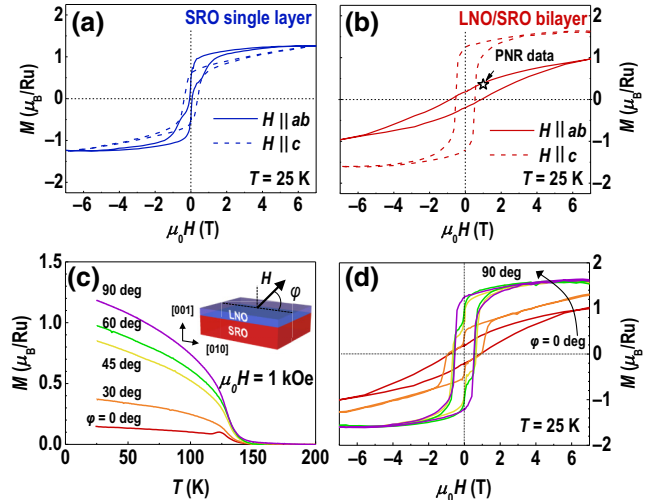


FIG. 2. Magnetometry measurements. (a), (b) Field-dependent magnetization of the SRO single layer and LNO/SRO bilayer, respectively. The magnetic field is applied along both in-plane ($H \parallel ab$) and out-of-plane ($H \parallel c$) directions. (c), (d) Temperature-dependent and field-dependent magnetization of the LNO/SRO bilayer, respectively. Magnetization measurements are performed when the magnetic field is applied at an angle of φ with respect to the sample's surface plane. Inset of (c) shows the geometry of magnetometry measurements with different magnetic field directions. M - T curves are collected during the sample warming up after field cooling at 1 kOe. M - H loops are measured at 25 K.

bilayer (approximately $1.67 \mu_B/\text{Ru}$). Magnetic anisotropy giving rise to the hysteresis loops is observed for both samples. The easy axis of a SRO single layer is the in-plane direction, which is different from other reports [46–48]. The magnetic anisotropy of SRO thin films is known to be complex. A slight change in the crystalline quality (twinning domains) and chemical stoichiometry during film growth may result in different types of crystalline anisotropy [46–48]. We note that the easy axis of the LNO/SRO bilayer is in the out-of-plane direction. The in-plane magnetization of the LNO/SRO bilayer is not saturated even for a magnetic field at 7 T. Apparently our results show the magnetic anisotropy of the SRO layer is changed by capping with an ultrathin LNO layer. The strong magnetic anisotropy of the LNO/SRO bilayer is further confirmed by conducting the magnetization measurements with rotational magnetic fields. As shown in the inset of Fig. 2(c), the schematic setup indicates the magnetic field is applied at an angle of φ with respect to the [010] plane of the sample. Figure 2(d) shows the squareness of the magnetic hysteresis loops becomes significant with increasing φ . When $\varphi = 30, 45,$ and 60° , the double hysteresis loops are observed in the LNO/SRO bilayer. The striking magnetic behavior suggests that the LNO/SRO bilayer may have different magnetic regions that respond differently as magnetic field increases.

Previous work showed the magnetic ground states depended on the interfacial structural symmetry by reversing the growth sequence [49]. Therefore, we investigate the structural and magnetic properties of a SRO layer with a LNO layer grown underneath (see Fig. S2 in the Supplemental Material [44]). The M_s and T_C of the LNO/SRO bilayer are almost the same as those of a SRO single layer, indicating the crystallographic symmetry and rotation pattern of the LNO ultrathin layer are similar to those of a STO substrate and have the same effect to the physical properties of SRO.

B. Enhanced electrical conductivity in the capped SRO ultrathin layer

The influence of the capping layer on electrical transport of the bilayer is investigated by comparing the temperature-dependent sheet resistances of the SRO single layer and the LNO/SRO bilayer (see Fig. S3 in the Supplemental Material [44]). The thickness of the LNO capping layer is only 6 u.c., and thus is expected to be highly insulating [50–53]. A kink in the $R-T$ curves at approximately 150 K, corresponding to the T_C of SRO, is observed in the $R-T$ curves of both the SRO single layer and the LNO/SRO bilayer. We find the T_C significantly reduces from 138 K for a SRO single layer to about 130 K for the LNO/SRO bilayer, which is consistent with our magnetization measurements [Fig. 2(c)]. The sheet resistance

of the LNO/SRO bilayer reduces to half of the SRO single layer's value. We also measured the sheet resistances of both samples at 7 T for $H||c$. The magnitude of magnetoresistances (MR) of the LNO/SRO bilayer is smaller than that of the SRO single layer. The reduction of resistivity and T_C in capped SRO is similar to the compressively strained SRO single layers [28,31,32], which is normally attributed to the structural-distortion-induced reduction of spin-dependent scattering. It is notable that the magnetic easy axis of the LNO/SRO bilayer aligns along the out-of-plane direction, and thus a smaller MR for the LNO/SRO bilayer is expected.

C. Identifying the magnetic origin in the LNO/SRO bilayer using XMCD and PNR

The magnetization depth profile across the LNO/SRO bilayer is determined quantitatively by PNR [54,55]. For the PNR experiment, we study an LNO/SRO bilayer with a LNO thickness of 25 u.c. (approximately 9 nm). The larger LNO thickness facilitates a larger scattering contrast. Magnetometer data indicate the LNO/SRO bilayers with different LNO thicknesses show the same magnetic anisotropy and saturation moment. As shown in the inset of Fig. 3(d), a maximum magnetic field of 1 T is applied along the in-plane direction during sample cooling and throughout the PNR measurements. Figure 3(a) shows the specular neutron reflectivity, R_{PNR} , of the LNO/SRO bilayer as a function of q at 25 K. PNR data are normalized to the asymptotic value of the Fresnel reflectivity, $R_F = 16\pi^2/q^4$. The open and solid symbols represent the reflectivities for the neutrons with spins parallel (R^+) or antiparallel (R^-)

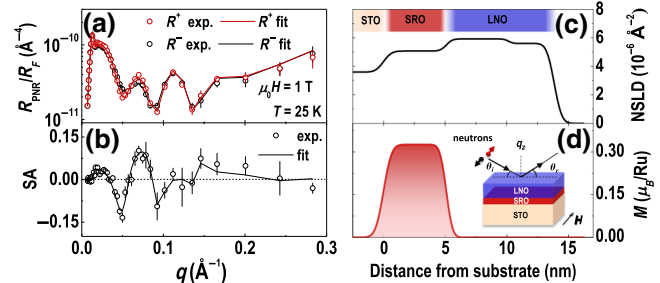


FIG. 3. PNR measurement. (a) Reflectivity curves for spin-up (R^+ , open circles) and spin-down (R^- , solid circles) polarized neutrons are plotted as a function of wave vector q . The reflectivity is normalized to the Fresnel reflectivity R_F . Dashed and solid lines are fitted curves to the experiment data. (b) Spin asymmetry [$\text{SA} = (R^+ - R^-)/(R^+ + R^-)$] derived from experiment data and fitted curves is plotted as a function of wave vector q . (c), (d) Neutron scattering-length density and magnetization depth profiles of the LNO/SRO bilayer, respectively. The magnetization is calculated from magnetic scattering-length density (MSLD) of the sample. Inset of (d) indicates the geometry of the PNR setup. PNR measurements are performed at 25 K under a magnetic field of 1 T. Magnetic field is applied along the in-plane direction.

to the applied field, respectively. The q -dependent splitting between the R^+ and R^- indicates the depth-dependent net moment in the LNO/SRO bilayer. Figure 3(b) shows the q -dependent SA. Open symbols represent the experimental data, the solid line is the best fit. Figures 3(c) and 3(d) show the nuclear scattering-length density (NSLD) and magnetization profiles of the LNO/SRO bilayer, respectively. We obtain $M_{\text{SRO}} = (0.36 \pm 0.02) \mu_B/\text{Ru}$, which agrees with the SQUID results shown in Fig. 2(b). From the PNR data, the magnetization exists exclusively in the SRO layer and the LNO layer does not have an in-plane-oriented magnetic moment.

Previous work has shown that interfacial interaction between transition metal oxides can induce a complex magnetic structure in a nonmagnetic material [56–59]. A profound interfacial magnetism in the paramagnetic LNO layers was reported in LNO/LaMnO₃ superlattices [56]. Therefore, the contribution of Ni ions to the overall magnetization of the LNO/SRO bilayer should be identified. We collect x-ray absorption spectroscopy (XAS) and x-ray magnetic circular dichroism (XMCD) spectra near the Ni L edges at 25 K (see Fig. S4 in the Supplemental Material [44]). The XAS spectra indicate the oxidization state of Ni ions is +3, indicating that charge transfer at the interfaces is negligible. Meanwhile, a nearly zero dichroic signal is observed at Ni L edges, consistent with a lack of moment in the LNO layers.

D. Structural transition and suppressed octahedral tilt in the LNO/SRO bilayer

To understand the correlation between the local structural variations and physical ground states of SRO layers, we perform the RSM and STEM ABF measurements on the SRO single layer and the LNO/SRO bilayer. From the RSM results in Fig. 4(a), we calculate the pseudocubic out-of-plane lattice parameter elongates to 3.95 Å for the SRO single layer, which is slightly larger than its bulk value (approximately 3.928 Å) [22] due to the substrate's in-plane compression. Although both samples are coherently strained to the STO substrate, the diffraction peak from the capped SRO layer shifts to a lower q_z , indicating the out-of-plane lattice parameter of the capped SRO layer increases to 3.971 Å. The RSMs around the substrate's (103) reflections of the SRO single layer are recorded by successively rotating the sample by 90° with respect to the film's surface normal. We observe the spacings of film peaks (marked by black arrows) with respect to the substrate's peak position are different in the SRO single layer [26]. After capping an ultrathin LNO layer on the SRO layer, the film's peak spacings are nearly identical [Fig. 4(b)]. These results suggest the structure of the SRO layer is distorted by changing crystallographic symmetry.

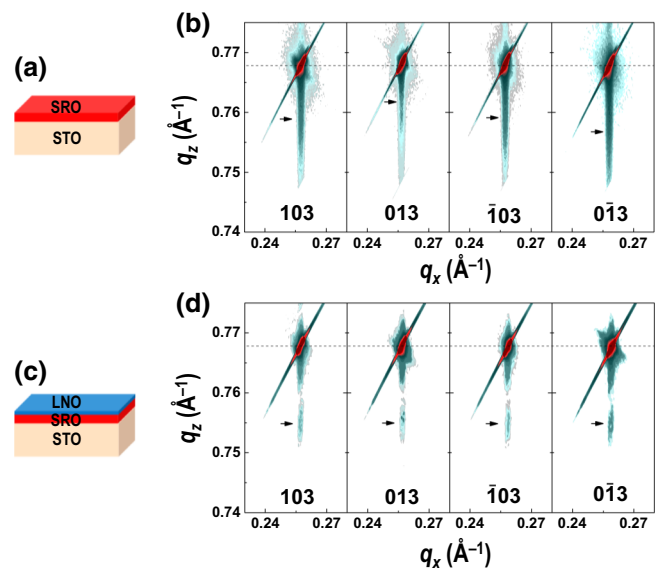


FIG. 4. Reciprocal space maps (RSMs) of an SRO single layer and a LNO/SRO bilayer. (a), (c) Schematics of a SRO single layer and a LNO/SRO bilayer, respectively. RSMs of (b) a SRO single layer and (c) a LNO/SRO bilayer, respectively. RSMs are taken around the substrate's 103 reflection are measured by azimuthally rotating the sample with a step size of 90° with respect to the surface's normal. All layers are coherently strained to the STO substrate with the same in-plane lattice parameter. The positions of the film's peak with maximum intensity are marked by black arrows in each panel.

More evidence of local structural distortion in SRO is provided by STEM characterizations. Figure 5(a) shows the ABF STEM image of a SRO single layer. The top layers with a thickness of 3–5 u.c. are damaged during the sample preparation and ion-milling process. We can determine that the SRO single layer exhibits a slightly tilted RuO₆ octahedra, as illustrated by the schematic in Fig. 5(b). In comparison, the RuO₆ octahedral tilt is strongly suppressed after the SRO layer is capped by an LNO layer [Figs. 5(d) and 5(e)]. We perform a quantitative analysis of ABF STEM images, which help us to probe the projection of oxygen atoms along the [100] zone. As shown in Fig. 5(b), we find that the RuO₆ octahedral tilt towards the in-plane direction and the tilt is opposite for the neighboring unit cells. Figure 5(c) shows the Ru—O—Ru bond angle $\beta_{\text{Ru}—\text{O}—\text{Ru}}$ is around $(174 \pm 1.8)^\circ$ in the SRO single layer. However, the averaged $\beta_{\text{Ru}—\text{O}—\text{Ru}}$ is close to space before and after 180° in the SRO layers after it is capped with LNO, inconsistent with that of $\beta_{\text{Ti}—\text{O}—\text{Ti}}$ in the STO substrate. We attribute the strong suppression of octahedral tilt in the SRO layer to being triggered by crystallographic symmetry change [22,60,61]. However, to explore the exact symmetry of ultrathin SRO layers is extremely difficult. The

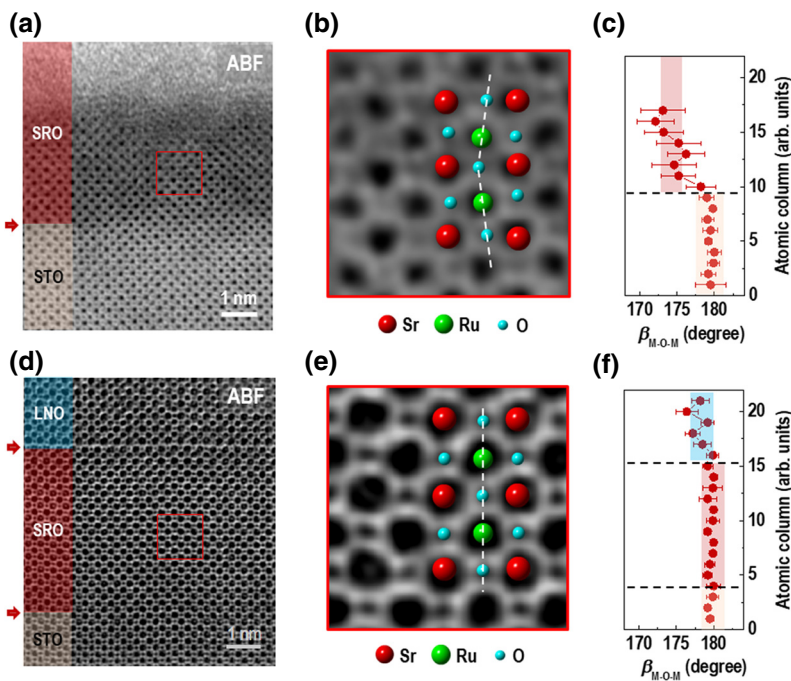


FIG. 5. Tetragonal SrRuO_3 ultrathin layer achieved by capping. (a), (d) ABF STEM images of a SRO single layer and a LNO/SRO bilayer grown on the STO substrate, respectively. (b), (e) Reduced ABF STEM images from the marked red square in (a), (d), respectively. The oxygen atoms are visible and the octahedra tilts in a SRO single layer, as indicated by the schematic in (b). However, no significant tilt of octahedra in SRO is observed after being capped with LNO. The $M\text{—}O\text{—}M$ bond angle $\beta_{M\text{—}O\text{—}M}$, where $M = \text{Ti}, \text{Ru}, \text{Ni}$, as a function of the atomic column, i.e., unit cell, are plotted in (c) a SRO single layer and (f) a LNO/SRO bilayer. The error bars correspond to the standard deviation of each $\beta_{M\text{—}O\text{—}M}$.

symmetry of a SRO ultrathin single layer could be monoclinic [30,46] or orthorhombic [59]. Both RSM and STEM results suggest the capped SRO layers are most likely to be the tetragonal structure. Similar results were reported earlier [62–65]. In the SRO single layers, the structural transition from the orthorhombic (or monoclinic) phase into a tetragonal phase was achieved at either high temperatures [62] or under a large tensile strain [63,64]. In the superlattices composed of $\text{Pr}_{0.7}\text{Ca}_{0.3}\text{MnO}_3$ and SrRuO_3 [65], the SRO interlayers were shown to change their crystal symmetry from the bulklike orthorhombic structure to a tetragonal variant when the PCMO layer thickness was increased from 1.5 to 4 nm. Our work provides an effective approach to modify the tetragonality of the SRO layer at the room temperature by adding an ultrathin capping layer.

Changing crystallographic symmetry modifies the octahedral parameters effectively. The SRO layers are coherently grown on the STO substrates, and thus the in-plane lattice parameter of SRO in both samples are the same. The STEM results clearly show the suppression of RuO_6 octahedral tilt after capping a LNO layer, resulting in the elongation of c -axis lattice parameter of SRO, consistent with RSM results. Early experiments have proven that anisotropic reduction in the orbital overlap in distorted octahedrons would lead to a strong anisotropic reduction in the crystal field. In our work, changes of the out-of-plane strain state alters the Ru spin configuration by changing the electron occupation of t_{2g} orbitals [33,34]. As shown in Figs. 2(a) and 2(b), the spin moment in SRO increases after capping a LNO, suggesting the magnitude of the t_{2g} splitting reduces. This simple model explains the enhanced M_s

observed in the LNO/SRO bilayer compared with that of a SRO single layer. Furthermore, the switching of magnetic anisotropy can be attributed to the crystallographic symmetry change of the SRO layer. Spin moments in SRO energetically favor being aligned along the out-of-plane direction in the tetragonal symmetry, resulting in an effective rotation of magnetic easy axis. This behavior is similar to earlier works [30,36,41]. By increasing the layer thickness of SRO, altering substrates with different rotation patterns, or heterostructuring underlayers with modified oxygen coordination environment, the magnetic easy axis of SRO rotates in response to the symmetry change. These observations demonstrate that the spin-orbital interaction of the SRO layer is sensitive to the small distortion in the octahedral structures. Finally, the enhancement of the conductivity in SRO layers originates from two contributions, spin-dependent scattering and electron correlation. Below the Curie temperature, spin-dependent scattering is reduced in the LNO/SRO bilayer when the magnetization is enhanced along the out-of-plane easy axis. Enhanced conductivity above the Curie temperature can be attributed to the reduction of electron correlation as a consequence of oxygen octahedral distortion. Therefore, the change of physical ground state in the capped SRO layers can be well explained by the distinct change of octahedral structural parameters.

IV. CONCLUSION

In summary, we show that a symmetry transition of the SRO layer with a suppressed octahedral tilt is achieved by capping SRO with an ultrathin nonmagnetic LNO layer.

This approach of interfacial structural modification is of general nature and can be extended easily to other perovskite oxides or strongly correlated materials with similar crystallographic structures. Our results thus open the possibility of tailoring the interfacial structure and lattice symmetry that has been inaccessible previously and suggest a tuning knob to explore the intriguing phenomena at the multifunctional oxide interfaces. In addition, our work also suggests the possibility of localized controlling the PMA in oxides with spatially patterned capping layer. This indicates the capability after the thin-film growth, which is inaccessible with previously reported substrate-based approaches.

ACKNOWLEDGMENT

E.J.G. is supported by the Hundred Talents Program from Chinese Academy of Sciences. M.R. acknowledges the use of facilities within the Eyring Materials Center at Arizona State University. This work is supported by the National Natural Science Foundation of China (Grant No. 11974390), the National Key R&D Program of China (Grants No. 2019YFA0308500 and No. 2017YFA0303604), and the Key Research Program of Frontier Sciences of the Chinese Academy of Sciences (Grant No. QYZDJ-SSW-SLH020). The research at ORNLs Spallation Neutron Source was sponsored by the Scientific User Facilities Division, BES, U.S. DOE.

-
- [1] G. Binasch, P. Grünberg, F. Saurenbach, and W. Zinn, Enhanced magnetoresistance in layered magnetic structures with antiferromagnetic interlayer exchange, *Phys. Rev. B* **39**, 4828 (1989).
 - [2] M. N. Baibich, J. M. Broto, A. Fert, F. Nguyen Van Dau, F. Petroff, P. Etienne, G. Creuzet, A. Friederich, and J. Chazelas, Giant Magnetoresistance of (001)Fe/(001)Cr Magnetic Superlattices, *Phys. Rev. Lett.* **61**, 2472 (1988).
 - [3] E. B. Myers, D. C. Ralph, J. A. Katine, R. N. Louie, and R. A. Buhrman, Current-Induced switching of domains in magnetic multilayer devices, *Science* **285**, 867 (1999).
 - [4] D. Chiba, M. Yamanouchi, F. Matsukura, and H. Ohno, Electrical manipulation of magnetization reversal in a ferromagnetic semiconductor, *Science* **301**, 943 (2003).
 - [5] P. Hai, S. Ohya, S. Barnes, S. Maekawa, and M. Tanaka, Electromotive force and huge magnetoresistance in magnetic tunnel junctions, *Nature* **458**, 489 (2009).
 - [6] C.-H. Lambert, S. Mangin, B. S. D. C. S. Varaprasad, Y. K. Takahashi, M. Hehn, M. Cinchetti, G. Malinowski, K. Hono, Y. Fainman, M. Aeschlimann, and E. E. Fullerton, All-optical control of ferromagnetic thin films and nanostructures, *Science* **345**, 1337 (2014).
 - [7] L. M. Loong, W. Lee, X. Qiu, P. Yang, H. Kawai, M. Saeys, J.-H. Ahn, and H. Yang, Flexible MgO barrier magnetic tunnel junction, *Adv. Mater.* **28**, 4983 (2016).
 - [8] C. D. Stanciu, F. Hansteen, A. V. Kimel, A. Kirilyuk, A. Tsukamoto, A. Itoh, and Th. Rasing, All-Optical Magnetic Recording with Circularly Polarized Light, *Phys. Rev. Lett.* **99**, 047601 (2007).
 - [9] Arne Brataas, Andrew D. Kent, and Hideo Ohno, Current-induced torques in magnetic materials, *Nat. Mater.* **11**, 372 (2012).
 - [10] X. Qiu, P. Deorani, K. Narayananpillai, K. Lee, K. Lee, H. Lee, and H. Yang, Angular and temperature dependence of current induced spin-orbit effective fields in Ta/CoFeB/MgO nanowires, *Sci. Rep.* **4**, 4491 (2014).
 - [11] N. Romming, et al., Writing and deleting single magnetic skyrmions, *Science* **341**, 636 (2013).
 - [12] P.-J. Hsu, A. Kubetzka, A. Finco, N. Romming, K. von Bergmann, and R. Wiesendanger, Electric-field-driven switching of individual magnetic skyrmions, *Nat. Nanotech.* **12**, 123 (2016).
 - [13] R. D. Desautels, L. DeBeer-Schmitt, S. A. Montoya, J. A. Borchers, S.-G. Je, N. Tang, M.-Y. Im, M. R. Fitzsimmons, E. E. Fullerton, and D. A. Gilbert, Realization of ordered magnetic skyrmions in thin films at ambient conditions, *Phys. Rev. Mater.* **3**, 104406 (2019).
 - [14] C. O. Avci, A. Quindeau, C. Pai, M. Mann, L. Caretta, A. S. Tang, M. C. Onbasli, C. A. Ross, and G. S. D. Beach, Current-induced switching in a magnetic insulator, *Nat. Mater.* **16**, 309 (2017).
 - [15] S. Vélez, J. Schaab, M. S. Wörnle, M. Müller, E. Gradauskaitė, P. Welter, C. Gutgsell, C. Nistor, C. L. Degen, M. Trassin, M. Fiebig, and P. Gambardella, High-speed domain wall racetracks in a magnetic insulator, *Nat. Commun.* **10**, 4750 (2019).
 - [16] Z. Qiu, T. An, K. Uchida, D. Hou, Y. Shiomi, Y. Fujikawa, and E. Saitoh, Experimental investigation of spin Hall effect in indium tin oxide thin film, *Appl. Phys. Lett.* **103**, 182404 (2013).
 - [17] I. Hajzadeh, B. Rahmati, G. R. Jafari, and S. M. Mohseni, Theory of the spin Hall effect in metal oxide structures, *Phys. Rev. B* **99**, 094414 (2019).
 - [18] J. Matsuno, et al., Interface-driven topological Hall effect in SrRuO₃-SrIrO₃ bilayer, *Sci. Adv.* **2**, e1600304 (2016).
 - [19] L. Wang, et al., Ferroelectrically tunable magnetic skyrmions in ultrathin oxide heterostructures, *Nat. Mater.* **17**, 1087 (2018).
 - [20] Q. Qin, L. Liu, W. Lin, X. Shu, Q. Xie, Z. Lim, C. Li, S. He, G. M. Chow, and J. S. Chen, Emergence of topological Hall effect in a SrRuO₃ single layer, *Adv. Mater.* **31**, 1807008 (2019).
 - [21] I. I. Mazin and D. J. Singh, Electronic structure and magnetism in Ru-based perovskites, *Phys. Rev. B* **56**, 2556 (1997).
 - [22] J. M. Rondinelli, N. M. Caffrey, S. Sanvito, and N. A. Spaldin, Electronic properties of bulk and thin film SrRuO₃: Search for the metal-insulator transition, *Phys. Rev. B* **78**, 155107 (2008).
 - [23] H. Wu, Y. G. Zhan, and W. Z. Shen, Quantum effect on SrRuO₃/BaTiO₃/SrRuO₃ ferroelectric ultrathin film capacitor, *Ferroelectrics* **401**, 246 (2010).
 - [24] H. Cheng, Z. Liu, and K. Yao, Rectifying behavior in La_{2/3}Sr_{1/3}MnO₃/MgO/SrRuO₃ magnetic tunnel junctions, *Appl. Phys. Lett.* **98**, 172107 (2011).
 - [25] R. Shiaa, H. Meng, and S. N. Piramanayagam, Materials with perpendicular magnetic anisotropy for magnetic

- random-access memory, *Phys. Status Solid RRL* **5**, 413 (2011).
- [26] A. Herklotz, M. Kataja, K. Nenkov, M. D. Biegalski, H.-M. Christen, C. Deneke, L. Schultz, and K. Doerr, Magnetism of the tensile-strain-induced tetragonal state of SrRuO₃ films, *Phys. Rev. B* **88**, 144412 (2013).
- [27] A. T. Zayak, X. Huang, J. B. Neaton, and Karin M. Rabe, Manipulating magnetic properties of SrRuO₃ and CaRuO₃ with epitaxial and uniaxial strains, *Phys. Rev. B* **77**, 214410 (2008).
- [28] Q. Gan, R. A. Rao, C. B. Eom, J. L. Garrett, and M. Lee, Direct measurement of strain effects on magnetic and electrical properties of epitaxial SrRuO₃ thin films, *Appl. Phys. Lett.* **72**, 978 (1998).
- [29] K. Terai, T. Ohnishi, M. Lippmaa, H. Koinuma, and M. Kawasaki, Magnetic properties of strain controlled SrRuO₃ thin films, *Jap. J. Appl. Phys.* **43**, 227 (2004).
- [30] M. Ziese, I. Vrejouw, and D. Hesse, Structural symmetry and magnetocrystalline anisotropy of SrRuO₃ films on SrTiO₃, *Phys. Rev. B* **81**, 184418 (2010).
- [31] D. Kan, R. Aso, H. Kurata, and Y. Shimakawa, Epitaxial strain effect in tetragonal SrRuO₃ thin films, *J. Appl. Phys.* **113**, 173912 (2013).
- [32] R. Aso, D. Kan, Y. Fujiyoshi, Y. Shimakawa, and H. Kurata, Strong dependence of oxygen octahedral distortions in SrRuO₃ films on types of substrate-induced epitaxial strain, *Crys. Growth Des.* **14**, 6478 (2014).
- [33] A. Grutter, F. Wong, E. Arenholz, M. Liberati, A. Vailionis, and Y. Suzuki, Enhanced magnetism in epitaxial SrRuO₃ thin films, *Appl. Phys. Lett.* **96**, 082509 (2010).
- [34] A. J. Grutter, F. Wong, E. Arenholz, A. Vailionis, and Y. Suzuki, Evidence of high-spin Ru and universal anisotropy in SrRuO₃ thin films, *Phys. Rev. B* **85**, 134429 (2012).
- [35] A. Vailionis, H. Bischker, W. Siemons, E. P. Houwman, D. H. A. Blank, G. Rijnders, and G. Koster, Misfit strain accommodation in epitaxial ABO₃ perovskites: Lattice rotations and lattice modulations, *Phys. Rev. B* **83**, 064101 (2011).
- [36] W. Lu, W. Song, P. Yang, J. Ding, G. M. Chow, and J. S. Chen, Strain engineering of octahedral rotations and physical properties of SrRuO₃ films, *Sci. Rep.* **5**, 10245 (2015).
- [37] D. Kan, M. Smada, Y. Wakabayashi, H. Tajiri, and Y. Shimakawa, Oxygen octahedral distortions in compressively strained SrRuO₃ epitaxial thin films, *J. Appl. Phys.* **123**, 235303 (2018).
- [38] J. M. Rondinelli and N. A. Spaldin, Structure and properties of functional oxide thin films: Insights from electronic-structure calculations, *Adv. Mater.* **23**, 3363 (2011).
- [39] E. J. Moon, P. V. Balachandran, B. J. Kirby, D. J. Keavney, R. J. Sichel-Tissot, C. M. Schleputz, E. Karapetrova, X. M. Cheng, J. M. Rondinelli, and S. J. May, Effect of interfacial octahedral behavior in ultrathin manganite films, *Nano Lett.* **14**, 2509 (2014).
- [40] Z. Liao, M. Huijben, Z. Zhong, N. Gauquelin, S. Macke, R. J. Green, S. Van Aert, J. Verbeeck, G. Van Tendeloo, K. Held, G. A. Sawatzky, G. Koster, and G. Rijnders, Controlled lateral anisotropy in correlated manganite heterostructures by interface-engineered oxygen octahedral coupling, *Nat. Mater.* **15**, 425 (2016).
- [41] D. Kan, R. Aso, R. Sato, M. Haruta, H. Kurata, and Y. Shimakawa, Tuning magnetic anisotropy by interfacially engineering the oxygen coordination environment in a transition metal oxide, *Nat. Mater.* **15**, 432 (2016).
- [42] S. Thomas, B. Kuiper, J. Hu, J. Smit, Z. Liao, Z. Zhong, G. Rijnders, A. Vailionis, R. Wu, G. Koster, and J. Xia, Localized Control of Curie Temperature in Perovskite Oxide Film by Capping Layer Induced Octahedral Distortion, *Phys. Rev. Lett.* **119**, 177203 (2017).
- [43] M. Gibert, M. Viret, A. Torres-Pardo, C. Piamanteze, P. Zubko, N. Jaouen, J. M. Tonnerre, A. Mougin, J. Fowlie, S. Catalano, A. Gloter, O. Stephan, and J. M. Triscone, Interfacial control of magnetic properties at LaMnO₃/LaNiO₃ interfaces, *Nano Lett.* **15**, 7355 (2015).
- [44] See Supplemental Material at <http://link.aps.org/supplemental/10.1103/PhysRevApplied.13.034033> for structural, electrical, and electronic state characterizations.
- [45] B. J. Kirby, P. A. Kienzle, B. B. Maranville, N. F. Berk, J. Krycka, F. Heinrich, and C. F. Majkrzak, Phase-sensitive specular neutron reflectometry for imaging the nanometer scale composition depth profile of thin-film materials, *Curr. Opin. Colloid Interface Sci.* **17**, 44 (2012).
- [46] S. Kolesnik, Y. Z. Yoo, O. Chmaissem, B. Dabrowski, T. Maxwell, C. W. Kimball, and A. P. Genis, Effect of crystalline quality and substitution on magnetic anisotropy of SrRuO₃ thin films, *J. Appl. Phys.* **99**, 08F501 (2006).
- [47] G. Herranz, F. Sanchez, N. Dix, D. Hrabovsky, I. C. Infante, J. Ontcuberta, M. V. Garcia-Cuenca, C. Ferrater, and M. Varela, Controlled magnetic anisotropy of SrRuO₃ thin films grown on nominally exact SrTiO₃ (001) substrates, *Appl. Phys. Lett.* **89**, 152501 (2006).
- [48] G. Koster, L. Klein, W. Siemons, G. Rijnders, J. Steven Dodge, C.-B. Eom, D. H. A. Blank, and Ma.R. Beasley, Structure, physical properties, and applications of SrRuO₃ thin films, *Rev. Mod. Phys.* **84**, 253 (2012).
- [49] S. J. May, J.-W. Kim, J. M. Rondinelli, E. Karapetrova, N. A. Spaldin, A. Bhattacharya, and P. J. Ryan, Quantifying octahedral rotations in strained perovskite oxide films, *Phys. Rev. B* **82**, 014110 (2010).
- [50] B. J. Kennedy and B. A. Hunter, High-temperature phases of SrRuO₃, *Phys. Rev. B* **58**, 653 (1998).
- [51] P. D. C. King, H. I. Wei, Y. F. Nie, M. Uchida, C. Adamo, S. Zhu, X. He, I. Božović, D. G. Schlom, and K. M. Shen, Atomic-scale control of competing electronic phases in ultrathin LaNiO₃, *Nat. Nanotech.* **9**, 443 (2014).
- [52] J. Son, et al., Low-dimensional mott material: Transport in ultrathin epitaxial LaNiO₃ films, *Appl. Phys. Lett.* **96**, 062114 (2010).
- [53] E. J. Guo, Y. Liu, C. Sohn, R. D. Desautels, A. Herklotz, Z. Liao, J. Nichols, J. W. Freeland, M. R. Fitzsimmons, and H. N. Lee, Oxygen diode formed in nickelate heterostructures by chemical potential mismatch, *Adv. Mater.* **30**, 1705904 (2018).
- [54] M. R. Fitzsimmons, S. D. Bader, J. A. Borchers, G. P. Felcher, J. K. Furdyna, A. Hoffmann, J. B. Kortright, I. K. Schuller, T. C. Schulthess, S. K. Sinha, M. F. Toney, D. Weller, and S. Wolf, Neutron scattering studies of nano-magnetism and artificially structured materials, *J. Mag. Mag. Mater.* **271**, 103 (2004).

- [55] C. F. Majkrzak, N. F. Berk, and U. A. Perez-Salas, Phase-sensitive neutron reflectometry, *Langmuir* **19**, 7796 (2003).
- [56] M. Gibert, P. Zubko, R. Scherwitzl, J. Íñiguez, and J.-M. Triscone, Exchange bias in LaNiO₃-LaMnO₃ superlattices, *Nat. Mater.* **11**, 195 (2012).
- [57] C. He, A. J. Grutter, M. Gu, N. D. Browning, Y. Takamura, B. J. Kirby, J. A. Borchers, J. W. Kim, M. R. Fitzsimmons, X. Zhai, V. V. Mehta, F. J. Wong, and Y. Suzuki, Interfacial Ferromagnetism and Exchange Bias in CaRuO₃/CaMnO₃ Superlattices, *Phys. Rev. Lett.* **109**, 197202 (2012).
- [58] J. Nichols, X. Gao, S. Lee, T. L. Meyer, J. W. Freeland, V. Lauter, D. Yi, J. Liu, D. Haskel, J. R. Petrie, E. J. Guo, A. Herklotz, D. Lee, T. Z. Ward, G. Eres, M. R. Fitzsimmons, and H. N. Lee, Emerging magnetism and anomalous hall effect in iridate–manganite heterostructures, *Nat. Commun.* **7**, 12721 (2016).
- [59] E. J. Guo, J. Petrie, M. Roldan, Q. Li, R. R. Desautals, T. Chalton, A. Herklotz, J. Nichols, J. van Lierop, J. W. Freeland, S. V. Kalinin, H. N. Lee, and M. R. Fitzsimmons, Spatially resolved large magnetization in ultrathin BiFeO₃, *Adv. Mater.* **29**, 1700790 (2017).
- [60] S. Thota, S. Ghosh, S. Nayak, D. C. Joshi, P. Pramanik, K. Roychowdhury, and S. Das, Finite-size scaling and exchange-bias in SrRuO₃/LaNiO₃/SrRuO₃ trilayers, *J. Appl. Phys.* **122**, 124304 (2017).
- [61] A. Herklotz, A. T. Wong, T. Meyer, M. D. Biegalski, H. N. Lee, and T. Z. Ward, Controlling octahedral rotations in a perovskite via strain doping, *Sci. Rep.* **6**, 26491 (2016).
- [62] K. J. Choi, S. H. Baek, H. W. Jang, L. J. Belenky, M. Lyubchenko, and C-B Eom, Phase-transition temperatures of strained single-crystal SrRuO₃ thin films, *Adv. Mater.* **22**, 759 (2010).
- [63] A. Vailionis, W. Siemons, and G. Koster, Room temperature epitaxial stabilization of a tetragonal phase in ARuO₃ (A = Ca and Sr) thin films, *Appl. Phys. Lett.* **93**, 051909 (2008).
- [64] S. Das, A. D. Rata, I. V. Maznichenko, S. Agrestini, E. Pippel, K. Chen, E. Pellegrin, S. M. Valvidares, H. B. Vasili, J. Herrero-Martin, K. Nenkov, A. Herklotz, A. Ernst, I. Mertig, Z. Hu, and K. Dörr, Low-field switching of noncollinear spin texture at La_{0.7}Sr_{0.3}MnO₃–SrRuO₃ interfaces, *Phys. Rev. B* **99**, 024416 (2019).
- [65] M. Ziese, I. Vrejoiu, E. Pippel, A. Hahnel, E. Nikulina, and D. Hesse, Orthorhombic-to-tetragonal transition of SrRuO₃ layers in Pr_{0.7}Ca_{0.3}MnO₃/SrRuO₃ superlattices, *J. Phys. D: Appl. Phys.* **44**, 345001 (2011).